Acta Crystallographica Section D
Biological Crystallography
ISSN 1399-0047

Structural basis for DNA recognition and nuclease processing by the Mre11 homologue SbcD in double-strand breaks repair

Shun Liu,[a,b]‡ Li-fei Tian,[a]‡ Yan-ping Liu,[a] Xiao-min An,[a] Qun Tang,[a] Xiao-xue Yan[a]* and Dong-cai Liang[a]*

[a]National Laboratory of Biomacromolecules, Institute of Biophysics, Chinese Academy of Sciences, Beijing 100101, People's Republic of China, and [b]University of Chinese Academy of Sciences, Beijing 100049, People's Republic of China

‡ SL and LT contributed equally to this work.

Correspondence e-mail: snow@moon.ibp.ac.cn, dcliang@sun5.ibp.ac.cn

Received 30 August 2013
Accepted 30 September 2013

PDB references: SbcD, 4lty; SbcD–Mn^{2+} complex, 4m0v

The Mre11 complex comprising meiotic recombination 11 (Mre11), Rad50 and Nijmegen breakage syndrome 1 (Nbs1) plays multiple important roles in the sensing, processing and repair of DNA double-strand breaks (DSBs). Here, crystal structures of the *Escherichia coli* Mre11 homologue SbcD and its Mn^{2+} complex are reported. Dimerization of SbcD depends on a four-helix bundle consisting of helices $\alpha2$, $\alpha3$, $\alpha2'$ and $\alpha3'$ of the two monomers, and the irregular and bent conformation of helices $\alpha3$ and $\alpha3'$ in the SbcD dimer results in a dimeric arrangement that differs from those of previously reported Mre11 dimers. This finding indicates a distinct selectivity in DNA substrate recognition. The biochemical data combined with the crystal structures revealed that the SbcD monomer exhibits single-stranded DNA (ssDNA) endonuclease activity and double-stranded DNA (dsDNA) exonuclease activity on the addition of a high concentration of Mn^{2+}. For the first time, atomic force microscopy analysis has been used to demonstrate that the SbcD monomer also possesses Mn^{2+}-dependent dsDNA endonuclease activity. Loop $\beta7$–$\alpha6$ of SbcD is likely to be a molecular switch and plays an important role in the regulation of substrate binding, catalytic reaction and state transitions. Based on structural and mutational analyses, a novel ssDNA-binding model of SbcD is proposed, providing insight into the catalytic mechanism of DSBs repair by the Mre11 complex.

1. Introduction

DNA double-strand breaks (DSBs) are a major danger to genome stability in all living creatures as they can cause chromosomal translocations and trigger tumourigenesis (Lee *et al.*, 2008; Putnam *et al.*, 2009; Wang *et al.*, 2009). DSBs require faithful repair to maintain genome stability and cell survival. Three pathways are involved in DSBs repair: homologous recombination (HR), nonhomologous end joining (NHEJ) and microhomology-mediated end joining (MMEJ).

The Mre11 complex consisting of Mre11, Rad50 and Nbs1 (or its functional homologue Xrs2 in *Saccharomyces cerevisae*) is the major sensor of DSBs. It recruits ataxia telangiectasia mutated protein (ATM) to impaired DNA ends and activates ATM to phosphorylate in turn members of the Mre11 complex and various related proteins involved in cell-cycle control and DNA repair (Lee & Paull, 2004, 2005). It also regulates DSBs repair through the HR, NHEJ and MMEJ pathways.

Homologues of Mre11 and Rad50 (but not Nbs1, which is only found in eukaryotes) exist widely in all species and are called SbcD and SbcC, respectively, in bacteria (Sharples &

Leach, 1995). The prokaryotic SbcCD complex shares common enzymatic activities and similar morphological character with the eukaryotic Mre11–Rad50 complex. The SbcCD complex is also important in the sensing, processing and repair of DSBs. SbcCD and PolX from *Deinococcus radiodurans* may play important complementary roles in processing damaged DNA ends (Bentchikou *et al.*, 2007). *Escherichia coli* SbcCD can transform single-stranded DNA (ssDNA) hairpin structures and protein-bound DNA ends produced during DNA replication to DSBs, which are repaired *via* HR (Connelly *et al.*, 1998, 1999, 2003). In the absence of SbcCD and RecA, a 246 bp DNA palindrome initiates the formation of large inverted chromosome duplications, suggesting that SbcCD and RecA protect the cell against DNA palindrome-induced chromosomal rearrangement (Darmon *et al.*, 2010).

The Mre11 complex comprises a large central globular domain, in which Mre11 and Nbs1 are associated with two ATPase domains of Rad50 called Walker A and Walker B, respectively. The crystal structure of *Pyrococcus furiosus* Mre11 (*Pf*Mre11) presents a protein phosphatase-like di-Mn^{2+}-binding domain capped by a unique domain controlling active-site access (Hopfner *et al.*, 2001). However, the bacterial Mre11 from *Thermotoga maritima* (*Tm*Mre11) with no metal ion bound in the nuclease activity site and lacking two additional β-strands compared with *Pf*Mre11 exhibits substantial differences in the DNA-specificity domain (capping domain) and its dimerization is mediated by a four-helix bundle (Das *et al.*, 2010). Human Mre11 (*Hu*Mre11) with two Mn^{2+} ions located in the active site assembles into a completely different dimeric architecture from its bacterial and archaeal homologues through interactions between a loop and a loop as well as between a loop and a helix (Park *et al.*, 2011). The structures of *Pf*Mre11 with synaptic DNA and branched DNA determined by small-angle X-ray scattering combined with crystallography revealed the roles of Mre11 in both DNA end bridging and nucleolytic processing during initiation of DSBs repair (Williams *et al.*, 2008). Recent insights into the structural features of the Mre11 complex demonstrated that the primary interactions between the C-terminal helix–loop–helix domain of Mre11 and the extended coiled-coil domain of Rad50 enable Mre11 to form a molecular clamp together with the N-terminal Walker A domain and the C-terminal Walker B domain of Rad50 in an open conformation in the absence of ATPγS and in a compact conformation in the presence of ATPγS (Lammens *et al.*, 2011; Lim *et al.*, 2011).

Mre11 consists of three regions: an N-terminal nuclease domain, a capping domain and a C-terminal region. The nuclease domain possesses strand-annealing activities and multiple nuclease activities, including 3′-to-5′ double-stranded DNA (dsDNA) exonuclease, ssDNA structure-specific endonuclease and hairpin nuclease activities (Connelly *et al.*, 1998; Paull & Gellert, 1998; Trujillo *et al.*, 1998; Hopfner *et al.*, 2000). The capping domain is important for substrate selectivity (Das *et al.*, 2010; Williams *et al.*, 2008). The helix–loop–helix domain of the C-terminal region can bind Rad50 and attach flexibly to the nuclease domain, enabling large conformational changes (Lammens *et al.*, 2011).

In this paper, we report the crystal structures of *E. coli* SbcD at 1.80 Å resolution and of the SbcD–Mn^{2+} complex at 1.83 Å resolution. Biochemical data confirmed that the SbcD monomer possesses broad Mn^{2+}-dependent nuclease activity. Based on biochemical assays and structural comparison, we propose an ssDNA-binding model for SbcD.

2. Materials and methods

2.1. Cloning and vector construction

Full-length *sbcD* (encoding residues 1–400; SbcD) and a fragment (encoding residues 1–340; $SbcD_{340}$) were amplified by PCR from *E. coli* genomic DNA and cloned into expression vector pET-28a with an N-terminal six-histidine tag. Mutations were produced by site-directed mutagenesis. Constructs were confirmed by DNA-sequencing analysis.

2.2. Protein expression and purification

E. coli BL21 (DE3) cells were used for the expression of all recombinant proteins. For SbcD (residues 1–400) and $SbcD_{340}$, the cells were grown in LB medium supplemented with 25 µg ml^{-1} kanamycin until the OD_{600} reached 0.6. Protein expression was induced by stimulation with 0.4 m*M* isopropyl β-D-1-thiogalactopyranoside (IPTG) at 28°C for 12–16 h. The cells were harvested, resuspended in lysis buffer (50 m*M* Tris pH 7.5, 400 m*M* NaCl, 0.1 m*M* EDTA, 5% glycerol, 5 m*M* β-mercaptoethanol) containing 20 m*M* imidazole and lysed by sonication. The lysate was clarified by centrifugation and purified using a nickel-affinity column. Further purification procedures were performed using a 120 ml Superdex 200 column (GE Healthcare) followed by a 6 ml Resource Q column (GE Healthcare). Purified SbcD and $SbcD_{340}$ proteins were stored in storage buffer (15 m*M* Tris pH 7.5, 100 m*M* NaCl, 0.1 m*M* EDTA, 5% glycerol, 1 m*M* 1,4-dithiothreitol) at concentrations of 33 and 35 mg ml^{-1}, respectively. The $SbcD_{340}$–Mn^{2+} complex was purified in buffers containing 1 m*M* $MnCl_2$ using the same procedures. The expression and purification procedures of SeMet-$SbcD_{340}$ and mutant variants were as the same as those used for SbcD.

2.3. Crystallization and data collection

SbcD failed to yield crystals, but crystals of $SbcD_{340}$ were grown using the hanging-drop vapour-diffusion method at 20°C by mixing 2 µl protein solution and 2 µl reservoir solution. Initial crystals were grown after 1 d using a reservoir solution consisting of 0.1 *M* HEPES–Na pH 7.5, 0.2 *M* lithium citrate, 24%(*w*/*v*) PEG 3350. Crystals suitable for X-ray diffraction studies were obtained by dynamic seeding after 3–5 d in conditions consisting of 0.1 *M* HEPES–Na pH 7.5, 0.16 *M* lithium citrate, 16%(*w*/*v*) PEG 3350. Crystals of SeMet-$SbcD_{340}$ and $SbcD_{340}$–Mn^{2+} were obtained using the same method as used for $SbcD_{340}$. The crystals were soaked in reservoir solution containing 20% glycerol for 2 min and flash-cooled in liquid nitrogen before data collection. Diffraction data sets were collected from the native and SeMet-derivative crystals on beamline BL17U at Shanghai Synchrotron

Table 1
Data-collection and refinement statistics.

Values in parentheses are for the highest resolution shell.

	SbcD	SbcD–Mn^{2+}	SeMet-SbcD
Data collection			
Wavelength (Å)	0.97917	0.97880	0.97916
Resolution range (Å)	50–1.80 (1.83–1.80)	50–1.83 (1.86–1.83)	50–2.50 (2.54–2.50)
Space group	*P*1	*P*1	*P*1
Unit-cell parameters			
a (Å)	62.1	62.2	61.8
b (Å)	69.4	69.2	69.4
c (Å)	95.0	95.2	94.7
α (°)	72.2	72.2	72.4
β (°)	84.1	84.0	84.2
γ (°)	83.8	83.5	83.7
Multiplicity	3.9 (3.9)	5.9 (6.0)	9.6 (9.4)
Completeness (%)	95.9 (95.3)	97.7 (96.3)	98.5 (97.8)
R_{merge} (%)	6.0 (35.6)	8.6 (81.0)	8.1 (39.6)
Mean $I/\sigma(I)$	36.0 (5.2)	34.7 (4.3)	35.9 (6.4)
Refinement			
Resolution (Å)	20–1.80	20–1.83	
No. of unique reflections	133164	128912	50747
R_{work}/R_{free} (%)	15.60/19.30	16.18/19.87	
No. of atoms			
Protein	10439	10442	
Ligand/ion	24	32	
Water	845	836	
B factors (Å^2)			
Protein	34.5	32.3	
Ligand/ion	30.1	36.2	
Water	40.1	38.5	
R.m.s. deviations			
Bond lengths (Å)	0.008	0.007	
Bond angles (°)	1.177	1.132	

Radiation Facility, People's Republic of China. Diffraction data sets were collected from the $SbcD_{340}$–Mn^{2+} crystals on beamline BL17A at Photon Factory, KEK, Japan. The data sets were integrated and scaled with *HKL*-2000 (Otwinowski & Minor, 1997). A statistical analysis of the data collection is summarized in Table 1.

2.4. Structure determination and refinement

The $SbcD_{340}$ structure (hereafter referred to as the SbcD structure) was determined at 1.80 Å resolution by single-wavelength anomalous dispersion (SAD). Using the initial phases calculated with *AutoSol* in the *PHENIX* software package (Adams *et al.*, 2010), an automatic model was built with the program *AutoBuild* in *PHENIX* at 2.5 Å resolution. Model refinement was performed in *PHENIX*. The program *Coot* (Emsley & Cowtan, 2004) was used for inspection and manual improvement of the model. The final model consisted of four SbcD molecules (named *A*, *B*, *C* and *D*), four glycerol molecules and 845 water molecules in the asymmetric unit. Residues 142–147, 296–300, 312–313 and 339–340 in molecule *C* were not modelled because of a poor electron-density map. Within the resolution range 20–1.80 Å, the native structure was refined to a final R_{work} of 15.60% and R_{free} of 19.30%. The Matthews coefficient (Matthews, 1968) is 2.44 Å^3 Da^{-1}, with an estimated solvent content of 49.24%(*v*/*v*). Acceptable stereochemistry was confirmed using a Ramachandran plot calculated by *PROCHECK* (Laskowski *et al.*, 1992). The Ramachandran plot showed that 96.9, 2.8 and 0.3% (four residues; His222 in each molecule) of the amino acids are in the favoured, allowed and outlier regions, respectively. His222 forms two pairs of hydrogen bonds to Thr186 and Arg197, resulting in its dihedral angle distribution being in the outlier region of the Ramachandran plot. The $SbcD_{340}$–Mn^{2+} structure (hereafter referred to as the SbcD–Mn^{2+} structure) was refined with the same strategy as used for SbcD. The statistics of the refinement of the final model are summarized in Table 1. The coordinates and structure factors of SbcD and the SbcD–Mn^{2+} complex have been deposited in the RCSB Protein Data Bank with accession codes 4lty and 4m0v, respectively.

2.5. Endonuclease assays

Endonucleolytic cleavage of circular single-stranded φX174 Virion DNA (New England Biolabs) was assayed with SbcD or $SbcD_{340}$ at 4, 25, 37 and 50°C and time points of 0 (control), 5, 10, 20 and 40 min. 5 µl reactions contained 1 µg circular φX174 DNA and 1 µ*M* purified protein (220 ng SbcD or 195 ng $SbcD_{340}$) in reaction buffer (25 m*M* HEPES pH 7.0, 25 m*M* NaCl, 5 m*M* $MnCl_2$). $MnCl_2$ was absent in the Mn^{2+} ion-free reactions. At the indicated time points, the reactions were stopped by the addition of EDTA to 20 m*M* and 1 µl 6× loading buffer. The reaction products were separated on 1.0% agarose gels in 1× TAE and visualized with Goldview staining. Assays with mutant variants were performed using the method described above.

2.6. Atomic force microscopy (AFM) analysis

The circular dsDNA substrate pQE30 plasmid DNA or protein, diluted to 1 ng µl^{-1} in reaction buffer, was spotted onto a freshly cleaved mica substrate. After 2 min at room temperature, the mica was washed three times with distilled water and dried under nitrogen. AFM observations were performed using a Nanoscope IIIa MultiMode system (Digital Instruments, Veeco, Santa Barbara, California, USA) in tapping mode in air. The ultrasharp NSC11/AIBS silicon cantilevers (MikroMasch, Tallinn, Estonia) used were 90 µm in length with a spring constant of ~48 N m^{-1}. The scanning frequency was 1 Hz and images were captured in height mode in a 512 × 512 pixel format. The obtained images were plane-fitted and flattened by the computer program accompanying the imaging module. 1 ng µl^{-1} pQE30 plasmid DNA and 1 ng µl^{-1} protein were mixed in reaction buffer. After incubation at 37°C for 10 min, the mixture was used in AFM observations using the method above.

2.7. Exonuclease assays

Steady-state 2-aminopurine (2-AP) fluorescence 3′–5′ exonuclease assays were performed on an F-7000 fluorescence spectrophotometer (Hitachi) with constant-wavelength excitation at 310 nm and emission monitored at 375 nm. An increase in the fluorescence at 375 nm was observed on the exonucleolytic release of 2-AP from the duplex DNA and was monitored over a period of 15 min for SbcD. Reactions (500 µl) consisted of 250 n*M* protein, 1 µ*M* 2-AP substrate,

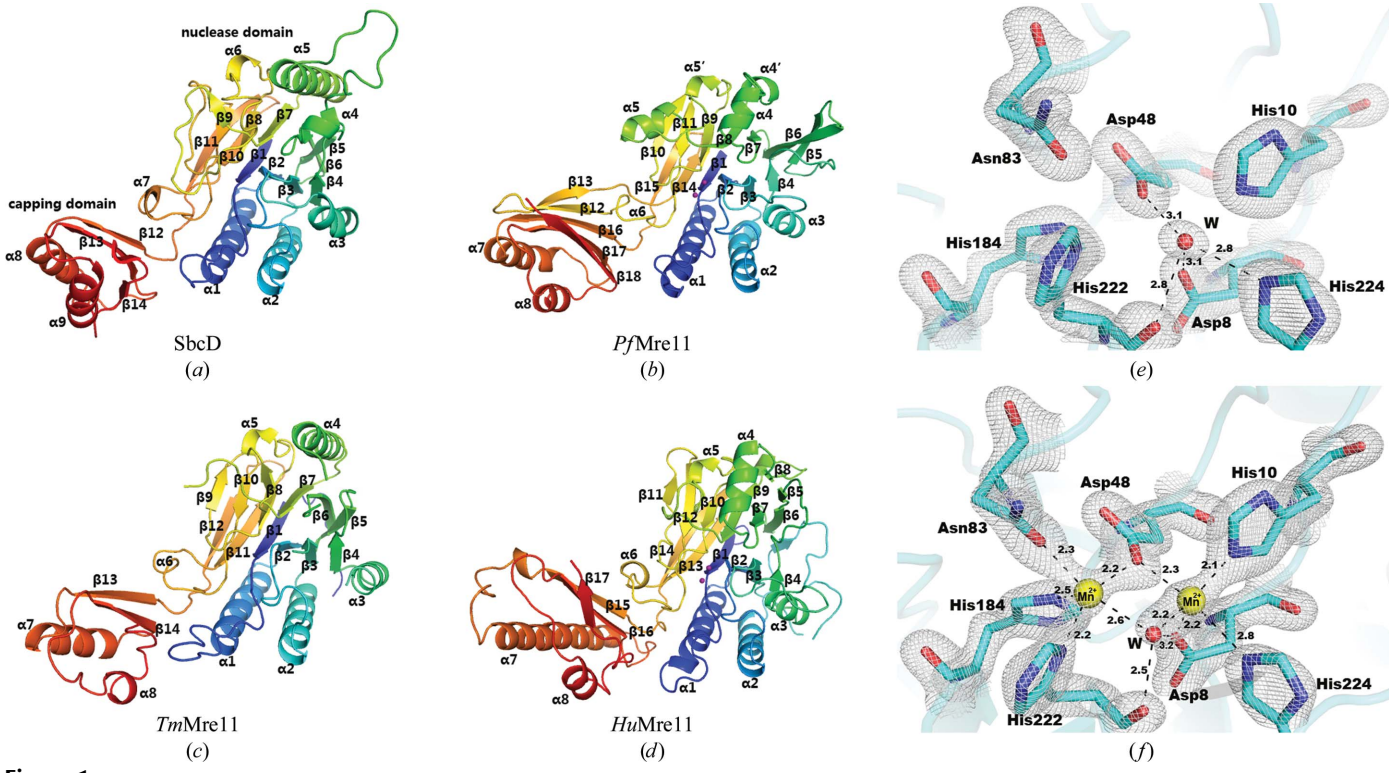

Figure 1
Structures of SbcD and other Mre11 monomers. (*a*)–(*d*) Structural comparison of SbcD with other Mre11 monomers: (*a*) SbcD, (*b*) *Pf*Mre11, (*c*) *Tm*Mre11 and (*d*) *Hu*Mre11. (*e*) The active site of SbcD. (*f*) The active site of SbcD–Mn^{2+}. In (*e*) and (*f*), the $2F_o - F_c$ electron density contoured at the 2.4σ level is shown as a grey mesh. Yellow and red spheres represent Mn^{2+} ions and water molecules (W), respectively. Interactions between atoms are depicted as black dashed lines; the unit of interatomic distance is Å.

50 m*M* Tris pH 7.5, 150 m*M* NaCl, 0.1% polyethylene glycol 6000, 2.5% glycerol, 1 m*M* $MnCl_2$. The reaction was tested at 37, 50 and 65°C. Blunt dsDNA substrate was formed by annealing equimolar amounts of exo1 [5′-GGCGTGCCTT-GGGCGCGCTGCGGGCGG(2-AP)G-3′] with exo2 (5′-CT-CCGCCCGCAGCGCGCCCAAGGCACGCC-3′). Reaction graphs were plotted by normalizing the fluorescence data for each reaction to the first data point.

2.8. Electrophoretic mobility shift assays (EMSA)

Circular single-stranded φX174 DNA and pQE30 plasmid DNA were used for ssDNA-binding and dsDNA-binding analyses, respectively. Various protein concentrations were incubated with φX174 DNA or pQE30 plasmid DNA in reaction buffer at room temperature for 15 min and the mixtures were separated on 1.0% agarose gels in 1× TAE and were visualized with Goldview staining.

3. Results and discussion

3.1. Three-dimensional structure of the SbcD monomer

$SbcD_{340}$ lacks 60 C-terminal residues; this does not affect the nuclease activity (Fig. 3*a*) but facilitates crystallization. The crystal of $SbcD_{340}$ belonged to space group *P*1 and the four molecules in the unit cell were very similar, with an r.m.s.d. of 0.5–0.6 Å over 340 C^{α} atoms. SbcD adopts a ladle-shaped architecture consisting of two α/β-fold domains, which are called the nuclease domain and the capping domain, respectively. A hinge connects the two domains. The nuclease domain is similar to calcineurin-like Ser/Thr phosphoesterase and comprises seven helices (α1–α7) and 11 strands (β1–β11; β5 and β10 are antiparallel to the other nine strands). The 11 strands are surrounded by helices α1, α2, α3 and α7 on one side and by helices α4, α5 and α6 on the other side, forming a β-sandwich. The capping domain is composed of three strands (β12–β14) packed by two helices (α8 and α9) on one face (Fig. 1*a* and Supplementary Fig. S1[1]). In the SbcD structure, the active site does not contain Mn^{2+} (Fig. 1*e*). However, we observed electron density for two Mn^{2+} ions in the SbcD–Mn^{2+} structure (Fig. 1*f*). The two Mn^{2+} ions are octahedrally coordinated by seven conserved residues of the active site (Asp8, His10, Asp48, Asn83, His184, His222 and His224) and by a bridging water molecule. Despite the binding of Mn^{2+}, the active-site residues in the SbcD–Mn^{2+} structure display the same conformation as those in the SbcD structure (Supplementary Fig. S2), indicating that both of the structures represent the substrate-free state of Mre11.

3.2. Comparison with other Mre11 structures

A comparison of the SbcD structure with the *Pf*Mre11 (PDB entry 1ii7; Hopfner *et al.*, 2001), *Tm*Mre11 (PDB entry 2q8u; Das *et al.*, 2010) and *Hu*Mre11 (PDB entry 3t1i; Park *et*

[1] Supporting information has been deposited in the IUCr electronic archive (Reference: DW5074).

al., 2011) structures (Figs. 1*a*–1*d*) shows that the nuclease domains share a similar architecture. However, the capping domains exhibit obviously different orientations because the hinge connecting the two domains is flexible, which is the architectural basis of the substantial conformational changes in the interaction with substrate.

The SbcD monomer possesses several unique features in comparison with the other Mre11 structures. Firstly, helix α3 of SbcD is irregular and bent, resulting in a different dimeric arrangement from the other Mre11 dimer structures. Secondly, α4 and loop α4–α5 are unique in the SbcD structure. Arg133 and Arg135 of α4 may participate in binding ssDNA. Thirdly, α5 in SbcD (α4 in the other Mre11 proteins) exhibits a different orientation from that in *Pf*Mre11 or *Hu*Mre11 and is comparatively longer than that in *Tm*Mre11. Fourthly, loop β7–α6 (residues 185–208) of SbcD is much longer than those in the other Mre11 proteins and has a different arrangement (Fig. 2*c*). The corresponding region of *Pf*Mre11 comprises loop β8–α5 (residues 174–176), α5 (residues 177–182) and loop α5–α5′ (residues 183–192), which is far from the active site. However, loop β7–α6 of SbcD clings onto the active site *via* hydrogen bonding from Thr186 and Arg197 to His222 (Fig. 2*d*). Accordingly, loop β7–α6 may play an important role in regulating SbcD nuclease activity.

Primary-sequence alignment analysis (Thompson *et al.*, 1994) between *Mj*Mre11 (the Mre11 protein from *Methanococcus jannaschii*), *Pf*Mre11, *Tm*Mre11, *Hu*Mre11 and SbcD revealed that Asp8, His10, Asp48, Asn83, His84, His184, His222 and His224 in the SbcD active site are conserved (Supplementary Fig. S3). The spatial arrangements of these conserved residues (Asn93 and His94 of *Tm*Mre11 are missing in the *Tm*Mre11 structure) at the active sites in SbcD and *Tm*Mre11 are strictly similar, indicating that SbcD and *Tm*Mre11 share an identical catalytic mechanism of nuclease

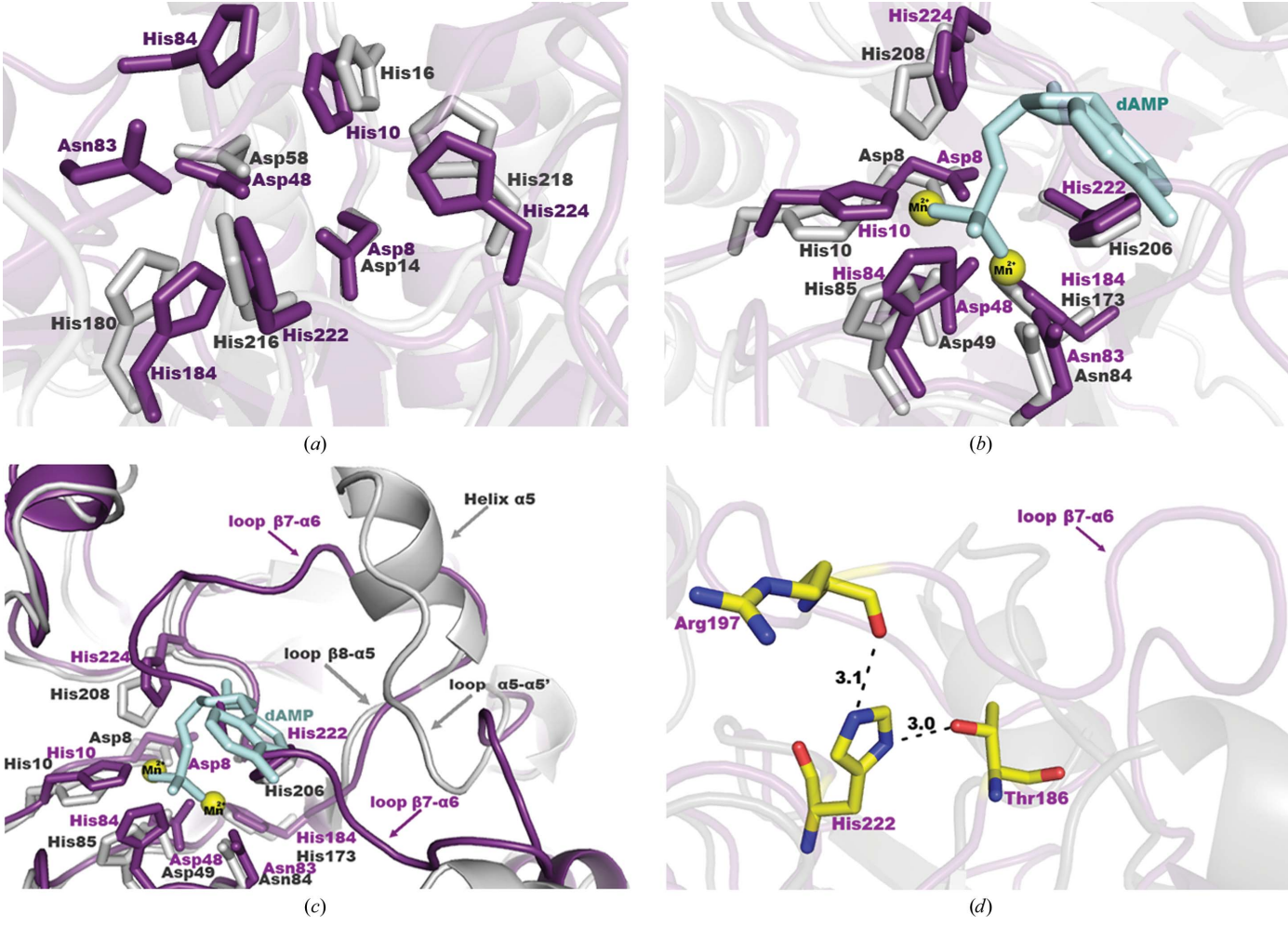

Figure 2
Structural comparison of the active site of SbcD with those of other Mre11 proteins. (*a*) Comparison of the active site of SbcD with that of *Tm*Mre11. Active-site residues in SbcD and *Tm*Mre11 are shown in purple and grey, respectively. (*b*) Comparison of the active site of SbcD with that of *Pf*Mre11–Mn^{2+}–dAMP. Active-site residues in SbcD and *Pf*Mre11 are shown in purple and grey, respectively. Yellow spheres represent Mn^{2+} ions. The dAMP molecule is shown in cyan. (*c*) Comparison of loop β7–α6 in SbcD with loop β8–α5, helix α5 and loop α5–α5′ in *Pf*Mre11. Loop β7–α6 in SbcD is shown in purple. Loop β8–α5, helix α5 and loop α5–α5′ in *Pf*Mre11 are shown in grey. Other elements are shown in the same colours as in (*b*). (*d*) Two pairs of hydrogen bonds formed between Thr186 and His222 and between Arg197 and His222 in SbcD (purple). *Pf*Mre11 is shown in grey. C atoms, O atoms and N atoms are shown in yellow, red and blue, respectively. Hydrogen bonds are depicted as black dashed lines. The unit of interatomic distance is Å.

activity and both show the apo form of Mre11 (Fig. 2*a*). A single mutation of the residues led to a complete loss of endonucleolytic activity (Fig. 3*d*), demonstrating that the active-site residues are necessary for nuclease activity.

Compared with the *Pf*Mre11 structure, the arrangement of the active-site residues of SbcD is more compact and the active-site residues His10, Asp48, His84 and His222 of SbcD shift by 1.2–1.9 Å towards the active centre with respect to His10, Asp49, His85 and His208 of *Pf*Mre11, respectively (Fig. 2*b*). Such a structural difference is mainly owing to the fact that *Pf*Mre11 contains two Mn^{2+} ions and one dAMP molecule in the active site. The *Pf*Mre11 structure containing Mn^{2+} and dAMP displays the substrate-bound state of Mre11. A short helix $\alpha5$ exists between loop $\beta8$–$\alpha5$ and loop $\alpha5$–$\alpha5'$ of *Pf*Mre11. It is distant from the active site and drives loop $\alpha5$–$\alpha5'$ to move backwards from the active site, providing sufficient space for the active site to accommodate dAMP molecules. Nevertheless, the corresponding region in SbcD exists as a long loop $\beta7$–$\alpha6$ (Fig. 2*c*). Two pairs of hydrogen bonds exist between the OG1 atom of Thr186 and the ND1 atom of His222, as well as between the carbonyl O atom of Arg197 and the NE2 atom of His222 (Fig. 2*d*). The two pairs of hydrogen bonds make loop $\beta7$–$\alpha6$ stick to the active site and forbid the binding of dAMP molecules by the active site. We

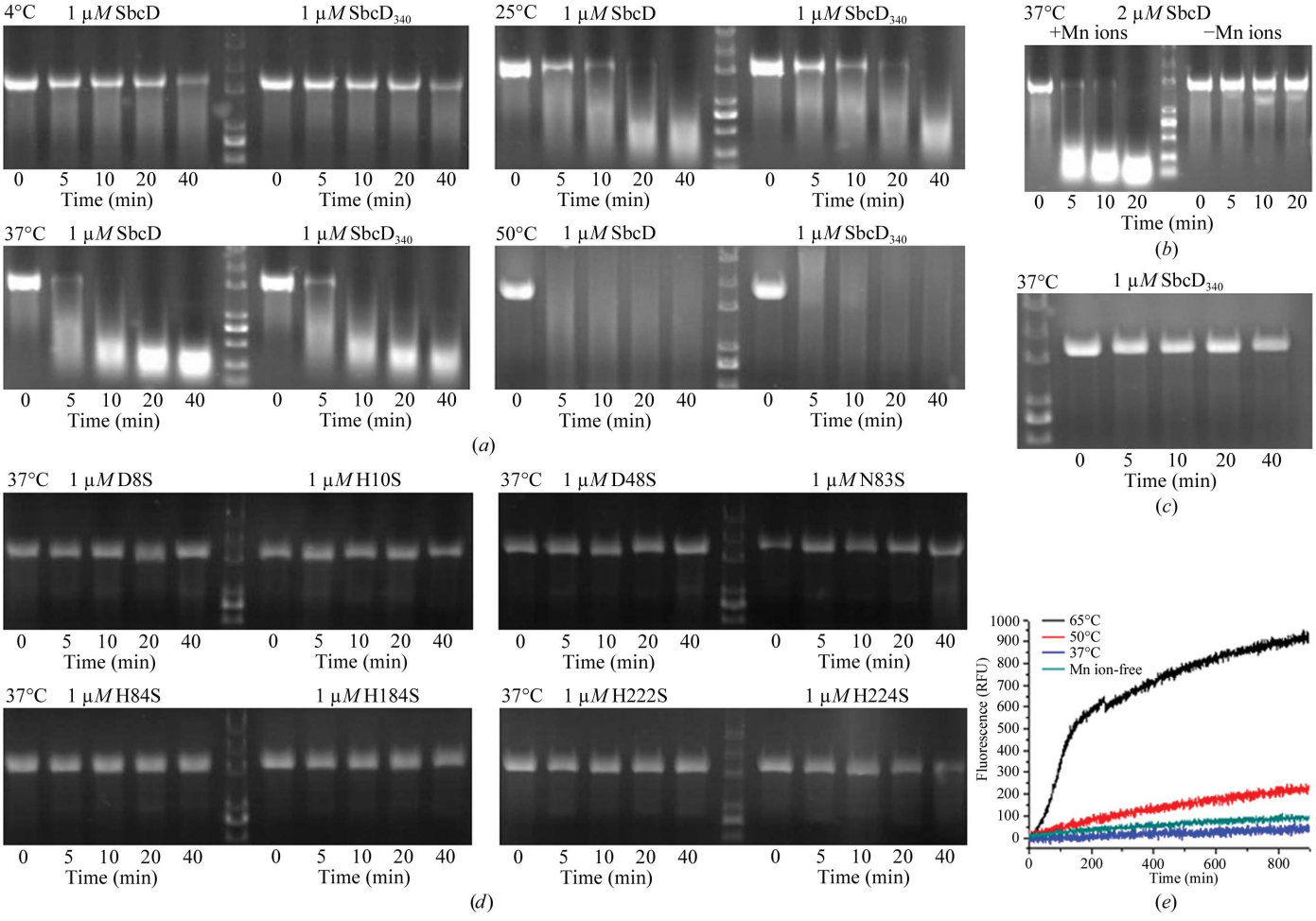

Figure 3
Nuclease assays of SbcD proteins. (*a*) Endonuclease assays of SbcD and $SbcD_{340}$ towards single-stranded bacteriophage φX174 DNA in the presence of Mn^{2+} at 4, 25, 37 and 50°C. The DNA standard is shown in the middle lane of each gel. Reactions containing SbcD and $SbcD_{340}$ are shown in the five lanes on the left and the right of the middle lane, respectively. The five lanes (from the left to the right) correspond to incubation times of 0 (no enzyme), 5, 10, 20 and 40 min, respectively. The reaction buffer contains Mn^{2+}. (*b*) Endonuclease assays of SbcD towards single-stranded bacteriophage φX174 DNA at 37°C in the presence and absence of Mn^{2+}. The DNA standard is shown in the middle lane. Reactions with and without Mn^{2+} are shown in the four lanes on the left and the right of the middle lane, respectively. The four lanes (from the left to the right) correspond to incubation times of 0 (no enzyme), 5, 10 and 20 min, respectively. (*c*) Endonuclease assays of $SbcD_{340}$ protein purified in buffers containing 1 m*M* $MnCl_2$ towards single-stranded bacteriophage φX174 DNA at 37°C in the absence of exogenous Mn^{2+}. The DNA standard is shown in the left lane. The other lanes (from the left to the right) correspond to incubation times of 0 (no enzyme), 5, 10, 20 and 40 min, respectively. (*d*) Endonuclease assays of SbcD variants with a single mutation in the active-site residues towards single-stranded bacteriophage φX174 DNA at 37°C. (*e*) Exonuclease assays of SbcD towards dsDNA substrate. The *x* axis of the reaction graph depicts the reaction time and the *y* axis depicts the fluorescence (relative fluorescence units; RFU) monitored during the release of 2-aminopurine base from the 2-aminopurine-modified dsDNA ascribed to exonuclease activity.

predict that loop $\beta7$–$\alpha6$ of SbcD is likely to be a molecular switch that plays an important role in regulating substrate binding, catalytic reaction and state transitions.

3.3. An SbcD monomer with a broad Mn^{2+}-dependent nuclease activity

Size-exclusion chromatography and analytical ultracentrifugation assays indicated that both SbcD and $SbcD_{340}$ are monomers in solution (Supplementary Fig. S4). Moreover, the crystal structure of SbcD shows that the SbcD monomer contains an integrated active centre that enables the monomer to efficiently exert its nuclease activity. Thus, we propose that the monomer is the functional unit of SbcD nuclease activity, in complete contrast to previous findings in which the dimer was considered to be the nuclease-activity functional unit of Mre11 (Hopfner *et al.*, 2001; Das *et al.*, 2010; Park *et al.*, 2011; Connelly *et al.*, 1997).

To determine the endonuclease activity of SbcD and $SbcD_{340}$, the activity of purified proteins towards bacteriophage φX174 ssDNA was assayed in the presence of 5 m*M* $MnCl_2$ at four different temperatures (4, 25, 37 and 50°C) and at different time points (Fig. 3*a*). The activity becomes stronger with increasing temperature. SbcD exhibits notable activity after incubation for 40 min even at 4°C, in contrast to *Pf*Mre11 and *Tm*Mre11, which exhibited no activity at 4°C (Hopfner *et al.*, 2001; Das *et al.*, 2010). $SbcD_{340}$ presents identical activity to SbcD at different temperatures, suggesting that the lack of the 60 C-terminal residues does not affect the endonuclease activity. In the absence of Mn^{2+} SbcD loses activity, which indicates that Mn^{2+} is required for endonuclease activity (Fig. 3*b*). Notably, $SbcD_{340}$–Mn^{2+} protein purified in buffers containing 1 m*M* $MnCl_2$ scarcely possesses any activity (Fig. 3*c*). The SbcD–Mn^{2+} structure reveals that in each SbcD molecule Mn^{2+} does not firmly bind to the active site of SbcD and the occupancy of Mn^{2+} is low. These findings suggest that the endonuclease activity of SbcD requires the presence of a high concentration (∼5 m*M*) of exogenous Mn^{2+}, indicating that SbcD possesses Mn^{2+}-dependent ssDNA endonuclease activity at different temperatures ranging from 4 to 50°C.

A fluorescence assay was performed to test the SbcD exonucleolytic release of 2-aminopurine from blunt dsDNA at 37, 50 and 65°C. Fluorescence emission data at 375 nm were collected for 15 min per reaction. The reaction at 37°C does not show any fluorescence, indicating that SbcD has no exonuclease activity at low temperatures (Fig. 3*e*). Moreover, SbcD shows weak activity at 50°C (Fig. 3*e*). At 65°C, a notable increase in fluorescence was observed over the period of data collection in the presence of 1 m*M* $MnCl_2$ (Fig. 3*e*). SbcD also displays no activity in the absence of Mn^{2+} at 65°C (Fig. 3*e*). These results indicated that SbcD exhibits Mn^{2+}-dependent dsDNA exonuclease activity at high temperatures, consistent with previous reports (Hopfner *et al.*, 2001; Das *et al.*, 2010).

The endonuclease activity of Mre11 towards dsDNA has not yet been reported. In this study, we used AFM to test the endonuclease activity of SbcD towards a circular dsDNA substrate. AFM analysis showed that the circular dsDNA substrate comprises only circular supercoils (Fig. 4*a*) and becomes linear DNA with visible tail ends after incubation with SbcD or $SbcD_{340}$ at 37°C for 10 min in the presence of Mn^{2+} (Figs. 4*b* and 4*c*). In the absence of Mn^{2+} both proteins can also bind dsDNA but fail to cut it

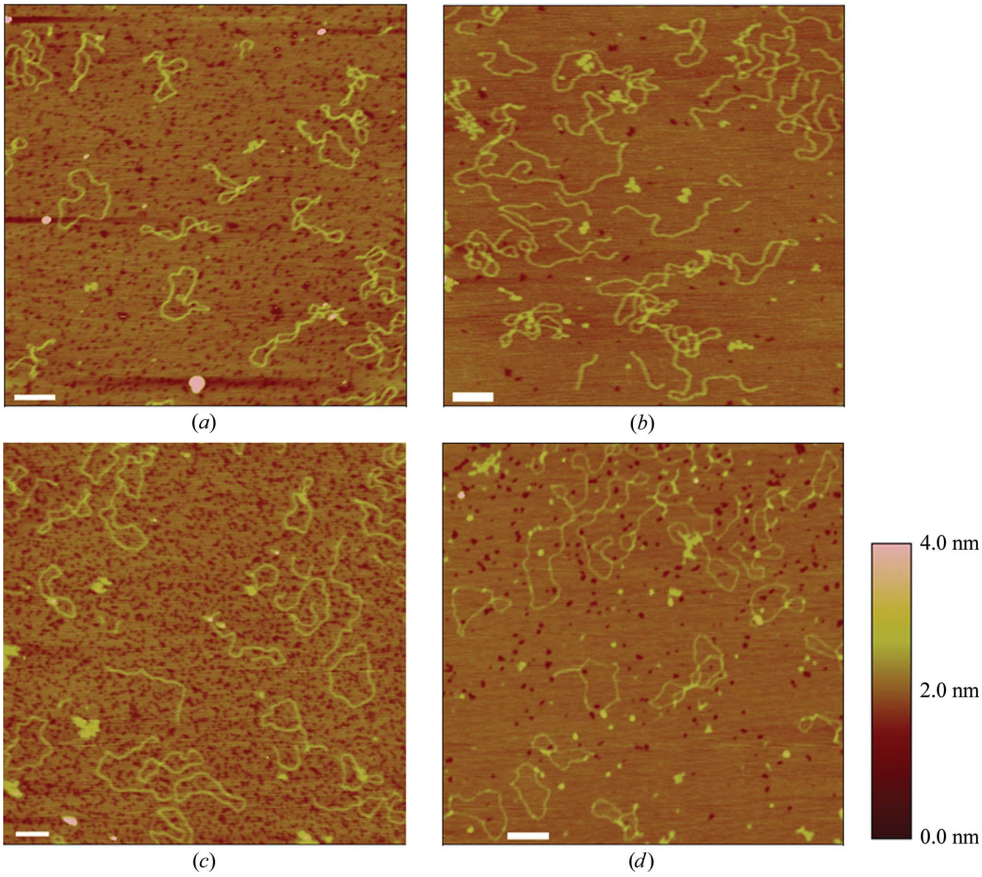

Figure 4
AFM analysis of SbcD endonuclease activity towards dsDNA. (*a*) Circular dsDNA (1 ng µl^{-1}). (*b*) A mixture of SbcD (1 ng µl^{-1}) and circular dsDNA (1 ng µl^{-1}) incubated at 37 °C for 10 min in the presence of Mn^{2+}. (*c*) A mixture of $SbcD_{340}$ (1 ng µl^{-1}) and circular dsDNA (1 ng µl^{-1}) incubated under the same conditions as in (*b*). (*d*) A mixture of SbcD (1 ng µl^{-1}) and circular dsDNA (1 ng µl^{-1}) incubated at 37°C for 10 min in the absence of Mn^{2+}. The scale bar is 200 nm in length. The colour bar represents the vertical height.

(Fig. 4*d*). For the first time, AFM analysis confirmed that SbcD possesses Mn^{2+}-dependent dsDNA endonuclease activity, which is not affected by the lack of the 60 C-terminal residues of SbcD.

3.4. The SbcD dimer probably participates in DSBs repair

Crystal-packing analysis of SbcD using *PISA* (Krissinel & Henrick, 2007) predicts that the four molecules in the unit cell give rise to two independent dimers composed of molecules *AC* and *BD* with a buried surface area of ∼1473 Å^2 per dimer (Fig. 5*a*). A four-helix bundle consisting of helices α2 and α3 of one monomer and helices α2′ and α3′ of the other monomer exists in the dimeric interface of SbcD. There is a noncrystallographic twofold symmetry axis in the two monomers. In each monomer, a pair of intramolecular salt bridges form between Arg60 of α2 and Glu92 of α3 and a pair of intramolecular hydrogen bonds form between Gln71 of α2 and Leu100 of α3. The salt bridges and hydrogen bonds play a critical role in stabilizing the conformation of α2 and α3 and even the entire monomer (Fig. 5*b*). In the dimeric interface, the following eight pairs of intermolecular hydrogen bonds exist: Ser57 (α2)–Glu92′ (α3′), Ser57 (α2)–Thr89′ (α3′), Asn64 (α2)–Glu92′ (α3′), Arg65 (α2)–Asp95′ (α3′) (two pairs), Ala88 (α3)–Ser57′ (α2′), Glu92 (α3)–Ser57′ (α2′) and Glu92 (α3)–Asn64′ (α2′) (Fig. 5*c*). Val68, Leu100, Ile96 and Phe99 of the two monomers in the dimeric interface are involved in intermolecular hydrophobic interactions (Fig. 5*d*). Intermolecular hydrogen bonds and hydrophobic interactions ensure the stabilization of the SbcD dimer.

Several studies (Hopfner *et al.*, 2001; Das *et al.*, 2010; Lammens *et al.*, 2011; Lim *et al.*, 2011; Park *et al.*, 2011) have reported that Mre11 proteins from different species exist in various oligomeric forms in solution. However, Mre11 proteins in a dimeric form bind to Rad50 and participate in DNA-damage repair. Hydrophobic interactions in the dimeric

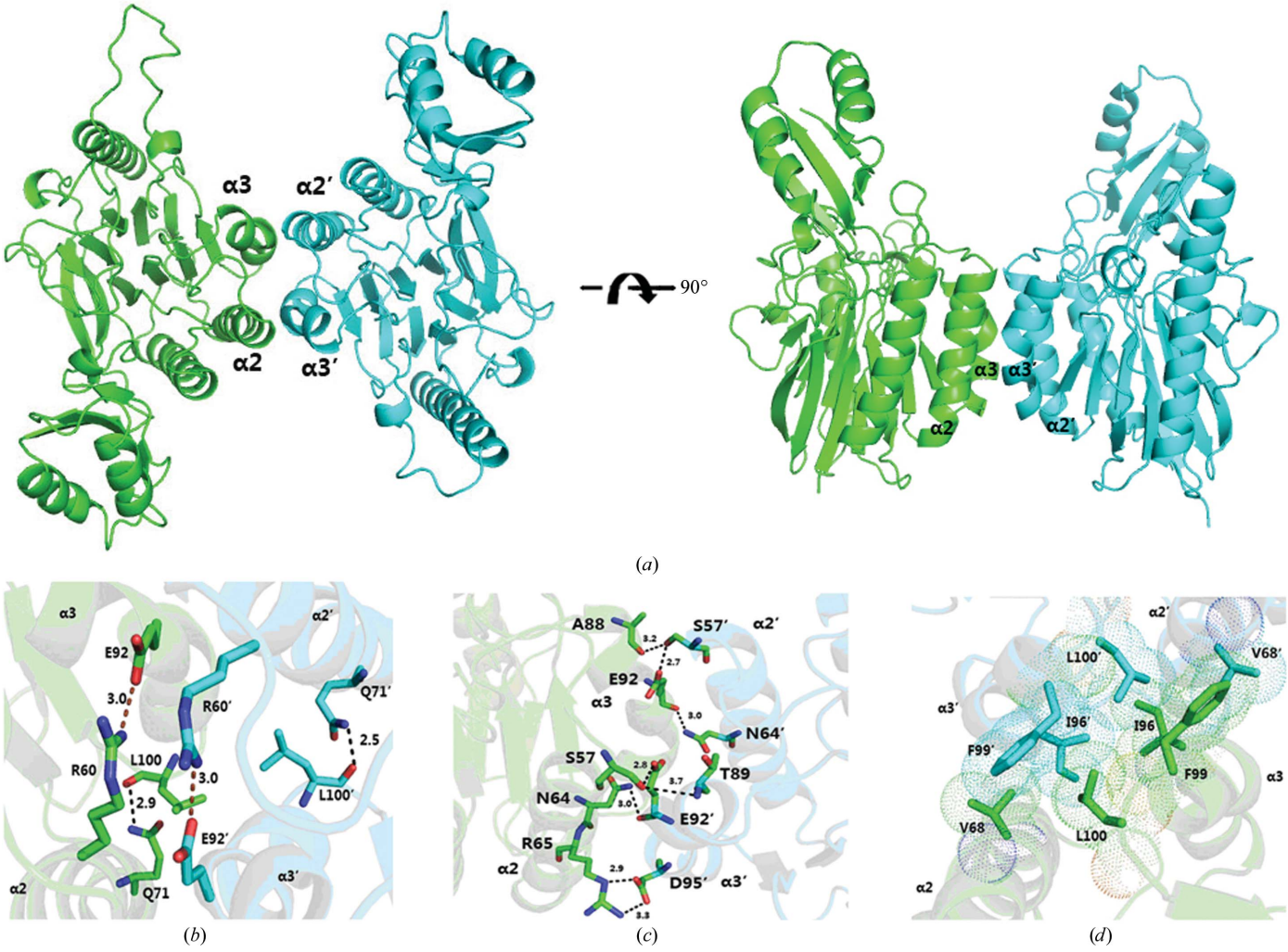

Figure 5
Architecture of the SbcD dimer. The two monomers are shown in green and cyan, respectively. (*a*) A four-helix bundle consisting of helices α2 and α3 of one monomer and helices α2′ and α3′ of the other monomer exists in the dimeric interface. (*b*) Intramolecular interactions in the dimeric interface. A pair of salt bridges (brown) are formed between Arg60 of helix α2 and Glu92 of helix α3 and a pair of hydrogen bonds (black) are formed between Gln71 of helix α2 and Leu100 of helix α3. (*c*) Eight pairs of intermolecular hydrogen bonds (black) in the dimeric interface. In (*b*) and (*c*) O atoms and N atoms are shown in red and blue, respectively. The unit of interatomic distance is Å. (*d*) Intermolecular hydrophobic interactions in the dimeric interface.

interface are essential for the high-precision assembly of the Mre11 dimer, which is critical not only for formation of the Mre11–Rad50 complex but also for the ATP hydrolysis activity of Rad50 (Williams *et al.*, 2008; Lim *et al.*, 2011). Our results showed that similar hydrophobic interactions exist in the SbcD dimer interface and mediate the dimerization of SbcD, which indicates that the SbcD dimer may be important for SbcCD complex formation and the ATP hydrolysis activity of SbcC. Moreover, eight pairs of hydrogen bonds (Fig. 5*c*) in the SbcD dimer interface play a key role in precise assembly of the SbcD dimer. Dimerization of Mre11 may enable the architectural DNA-binding functions of the Mre11 complex by promoting high-affinity DNA interactions (Williams *et al.*, 2008). Accordingly, we predicted that SbcD in the form of a dimer interacts with SbcC, binds various DNA structures and exerts broad nuclease activities towards different DNA substrates.

The Mre11 capping domain participates in Rad50 binding (Lammens *et al.*, 2011), and interactions between the capping domain and Rad50 have been associated with the endonuclease activity of Mre11 (Lim *et al.*, 2011). A comparison of the SbcD dimer with the *Tm*Mre11 dimer *via* one monomer (Supplementary Fig. S5) revealed that differences in the orientation of the capping domain of the other monomer between the two dimers are apparent and that the deviation angle between the two capping domains is approximately 25° with respect to the centre of the dimeric interface. The capping domains of the SbcD dimer are closer to the dimeric interface

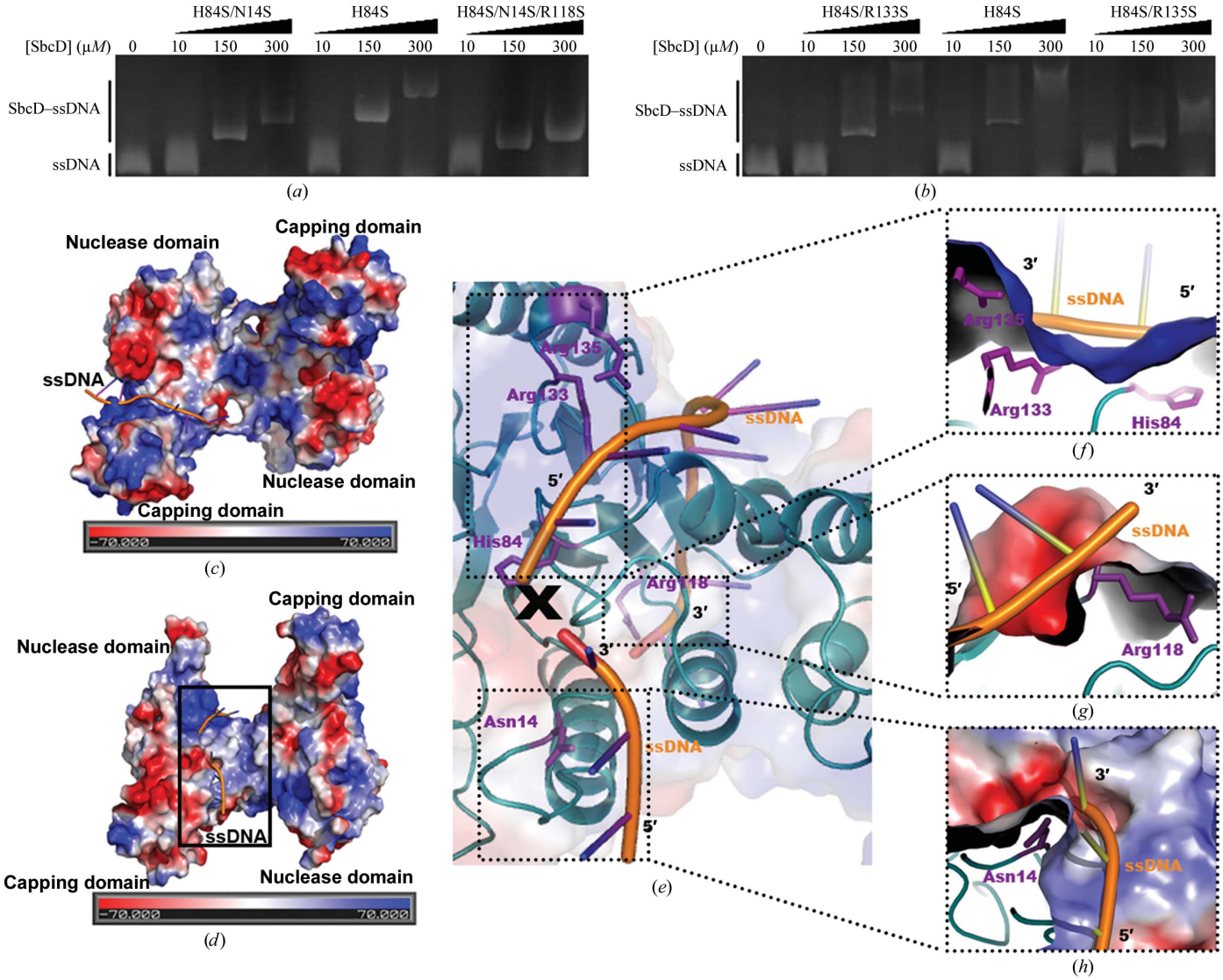

Figure 6
Interactions between ssDNA and Mre11 dimers. (*a*) ssDNA-binding activity of $SbcD_{H84S/N14S}$ and $SbcD_{H84S/N14S/R118S}$. (*b*) ssDNA-binding activity of $SbcD_{H84S/R133S}$ and $SbcD_{H84S/R135S}$. (*c*) Proposed ssDNA-binding model of the *Pf*Mre11 dimer. (*d*) Proposed ssDNA-binding model of the SbcD dimer. (*e*) ssDNA-binding model of the SbcD dimer shown as a cartoon. The X represents where SbcD cuts ssDNA. (*f*) Interactions between ssDNA and His84, Arg133 and Arg135 of SbcD. (*g*) Interactions between ssDNA and Arg118 of SbcD. (*h*) Interactions between ssDNA and Asn14 of SbcD. In (*c*)–(*h*) the surface of the proteins is coloured by electrostatic potential, with red representing electronegative regions and blue representing electropositive regions.

than those of the *Tm*Mre11 dimer, forming a more compact structure. Each helix in the *Tm*Mre11 dimer interface is a regular α-helix. In contrast, in the SbcD dimer the interface helices $\alpha2$ and $\alpha2'$ are regular but helices $\alpha3$ and $\alpha3'$ are irregular and remarkably bent. We predicted that the irregular and bent conformation of helices $\alpha3$ and $\alpha3'$ shortens the distance between the two SbcD monomers, resulting in apparent differences in the orientation of the capping domain of the other monomer between the two dimers and in a more compact structure of the SbcD dimer than of the *Tm*Mre11 dimer. The capping domain is very important for substrate selectivity (Das *et al.*, 2010; Williams *et al.*, 2008). Thus, the differences in the orientation of the capping domain between the SbcD dimer and the *Tm*Mre11 dimer indicate the possibility that the substrate specificity may differ between the two dimers even though both of them are from bacteria.

3.5. DNA-binding models of SbcD

The crystal structures of the *Pf*Mre11–synaptic DNA complex (PDB entry 3dsc) and the *Pf*Mre11–branched DNA complex (PDB entry 3dsd) revealed that 17 residues participate in DNA binding (Williams *et al.*, 2008). Primary-sequence alignment analysis (Supplementary Fig. S3) shows that the conserved residues Asn14, Tyr16, Lys18, Arg118 and Arg339 in SbcD correspond to the DNA-binding residues Glu14, Phe16, Lys18, Lys111 and Lys327 in *Pf*Mre11, respectively, and probably play an important role in the recognition of ssDNA, dsDNA and DNA hairpin structures. Superposition of SbcD with *Pf*Mre11–DNA structures (Supplementary Figs. S6*b* and S6*c*) reveals that synaptic DNA interacts with Asn14 and Lys18 in SbcD, whereas branched DNA interacts with Lys18 in SbcD. Thus, Asn14 and Lys18 of SbcD may bind dsDNA.

Based on the structure of SbcD, we performed a mutational analysis. The interactions of the $SbcD_{H84S/N14S}$, $SbcD_{H84S/N14S/R118S}$ and $SbcD_{H84S/R339S}$ variants with dsDNA were assayed by EMSA (Supplementary Fig. S6*a*). Conforming with our predictions, $SbcD_{H84S}$ loses the nuclease activity (Fig. 3*d*) but still binds dsDNA. The dsDNA-binding ability of $SbcD_{H84S/N14S}$ is weaker than that of $SbcD_{H84S}$ and the dsDNA-binding ability of $SbcD_{H84S/N14S/R118S}$ is weaker than that of $SbcD_{H84S/N14S}$, which indicates that both Asn14 and Arg118 participate in the dsDNA binding of SbcD. In addition, dsDNA incubated with $SbcD_{H84S/R339S}$ migrates at the same rate as $SbcD_{H84S}$, suggesting that Arg339 is not the dsDNA-binding site of SbcD. Accordingly, we speculated on the binding mode of SbcD to dsDNA (Supplementary Fig. S6*e*). When DSBs occur, SbcD accumulates in the form of a dimer at the impaired DNA ends. Upon rotation of the capping domain, Asn14 and Arg118 bind to dsDNA and stabilize the DNA ends for subsequent repair.

Using docking, Williams and coworkers identified the ssDNA-binding sites in *Pf*Mre11 (Fig. 6*c*) to be located at the capping–nuclease domain interface (Williams *et al.*, 2008). The electrostatic surface potential of SbcD reveals that the active-site residue His84 forms a positive-charged groove together with Arg133 and Arg135 near the active site (distant from the capping–nuclease domain interface). We suppose that this groove is the ssDNA-binding site of SbcD (Figs. 6*d* and 6*e*). EMSA analyses of the $SbcD_{H84S/R133S}$ (Fig. 6*b*), $SbcD_{H84S/R135S}$ (Fig. 6*b*), $SbcD_{H84S/N14S}$ and $SbcD_{H84S/N14S/R118S}$ (Fig. 6*a*) variants suggest that Arg133 and Arg135 are involved in ssDNA binding, consistent with the conclusion resulting from the analysis of the surface electrostatic potential map of SbcD. Moreover, Asn14 and Arg118 also participate in interactions with ssDNA. Thus, we proposed a novel ssDNA-binding model of SbcD (Figs. 6*d* and 6*e*) in which Arg118, Arg133 and Arg135 together with Asn14 on the other side of the active site bind ssDNA, and His84, together with other active-site residues, exerts the endonuclease activity to cut the ssDNA. SbcD possesses significantly distinct ssDNA-binding sites from *Pf*Mre11, suggesting that the endonucleolytic mechanism of SbcD towards ssDNA may differ from that of *Pf*Mre11.

In summary, our structural and biochemical data on SbcD reveal several distinct features from other Mre11 proteins and provide a novel foundation for understanding the interactions of SbcD with ssDNA. More concrete structures and relative investigations are required to elucidate the mechanism of DSBs repair by the Mre11 complex.

We thank the staff at the Shanghai Synchrotron Radiation Facility (beamline BL17U; Project No. 12SRBL17U11510) and the Photon Factory, KEK (beamline BL-1A; Project No. 2013G061) for their kind help in data collection. We thank Drs Yan-xia Jia, Xiao-xia Yu and Hong-mei Zhang of the IBP for technical assistance and helpful discussion. We also thank Ming-xing Chen of Peking University for assistance in fluorescence data collection. This work was supported by grants from the National Natural Science Foundation of China (Nos. 31070684 and 31371310), the Major State Basic Research Development Program of China (973 Program; Nos. 2011CB910302, 2011CB966303 and 2011CB911101) and the Institute of Biophysics, Chinese Academy of Sciences.

References

Adams, P. D. *et al.* (2010). *Acta Cryst.* D**66**, 213–221.
Bentchikou, E., Servant, P., Coste, G. & Sommer, S. (2007). *J. Bacteriol.* **189**, 4784–4790.
Connelly, J. C., de Leau, E. S. & Leach, D. R. (1999). *Nucleic Acids Res.* **27**, 1039–1046.
Connelly, J. C., de Leau, E. S. & Leach, D. R. (2003). *DNA Repair*, **2**, 795–807.
Connelly, J. C., de Leau, E. S., Okely, E. A. & Leach, D. R. (1997). *J. Biol. Chem.* **272**, 19819–19826.
Connelly, J. C., Kirkham, L. A. & Leach, D. R. (1998). *Proc. Natl Acad. Sci. USA*, **95**, 7969–7974.
Darmon, E., Eykelenboom, J. K., Lincker, F., Jones, L. H., White, M., Okely, E., Blackwood, J. K. & Leach, D. R. (2010). *Mol. Cell*, **39**, 59–70.
Das, D. *et al.* (2010). *J. Mol. Biol.* **397**, 647–663.
Emsley, P. & Cowtan, K. (2004). *Acta Cryst.* D**60**, 2126–2132.
Hopfner, K. P., Karcher, A., Craig, L., Woo, T. T., Carney, J. P. & Tainer, J. A. (2001). *Cell*, **105**, 473–485.
Hopfner, K. P., Karcher, A., Shin, D., Fairley, C., Tainer, J. A. & Carney, J. P. (2000). *J. Bacteriol.* **182**, 6036–6041.
Krissinel, E. & Henrick, K. (2007). *J. Mol. Biol.* **372**, 774–797.

Lammens, K., Bemeleit, D. J., Möckel, C., Clausing, E., Schele, A., Hartung, S., Schiller, C. B., Lucas, M., Angermüller, C., Söding, J., Strässer, K. & Hopfner, K. P. (2011). *Cell*, **145**, 54–66.
Lee, J.-H. & Paull, T. T. (2004). *Science*, **304**, 93–96.
Lee, J.-H. & Paull, T. T. (2005). *Science*, **308**, 551–554.
Lee, K., Zhang, Y. & Lee, S. E. (2008). *Nature (London)*, **454**, 543–546.
Lim, H. S., Kim, J. S., Park, Y. B., Gwon, G. H. & Cho, Y. (2011). *Genes Dev.* **25**, 1091–1104.
Laskowski, R. A., MacArthur, M. W., Moss, D. S. & Thornton, J. M. (1993). *J. Appl. Cryst.* **26**, 283–291.
Matthews, B. W. (1968). *J. Mol. Biol.* **33**, 491–497.
Otwinowski, Z. & Minor, W. (1997). *Methods Enzymol.* **276**, 307–326.
Park, Y. B., Chae, J., Kim, Y. C. & Cho, Y. (2011). *Structure*, **19**, 1591–1602.
Paull, T. T. & Gellert, M. (1998). *Mol. Cell*, **1**, 969–979.
Putnam, C. D., Hayes, T. K. & Kolodner, R. D. (2009). *Nature (London)*, **460**, 984–989.
Sharples, G. J. & Leach, D. R. (1995). *Mol. Microbiol.* **17**, 1215–1217.
Thompson, J. D., Higgins, D. G. & Gibson, T. J. (1994). *Nucleic Acids Res.* **22**, 4673–4680.
Trujillo, K. M., Yuan, S.-S. F., Lee, E. Y.-H. P. & Sung, P. (1998). *J. Biol. Chem.* **273**, 21447–21450.
Wang, J. H., Gostissa, M., Yan, C. T., Goff, P., Hickernell, T., Hansen, E., Difilippantonio, S., Wesemann, D. R., Zarrin, A. A., Rajewsky, K., Nussenzweig, A. & Alt, F. W. (2009). *Nature (London)*, **460**, 231–236.
Williams, R. S., Moncalian, G., Williams, J. S., Yamada, Y., Limbo, O., Shin, D. S., Groocock, L. M., Cahill, D., Hitomi, C., Guenther, G., Moiani, D., Carney, J. P., Russell, P. & Tainer, J. A. (2008). *Cell*, **135**, 97–109.